

Article

# Ultrafast Heating and Initial Microstructure Effect on Phase Transformation Evolution of a CrMo Steel

Spyros Papaefthymiou <sup>1,\*</sup> , Vassilios Karamitros <sup>1,\*</sup>  and Marianthi Bouzouni <sup>1,2</sup>

<sup>1</sup> National Technical University of Athens, School of Mining and Metallurgical Engineering, Division of Metallurgy and Materials, Laboratory of Physical Metallurgy, 9, Her. Polytechniou str., Zografos, 15780 Athens, Greece; mbouzouni@elkeme.vionet.gr

<sup>2</sup> Hellenic Research Centre for Metals (ELKEME S.A.), Department of Physical Metallurgy and Forming, 61st km Athens—Lamia Nat. Road, 32011 Oinofyta, Viotia, Greece

\* Correspondence: spapaef@metal.ntua.gr (S.P.); v.karamitros18@imperial.ac.uk (V.K.); Tel.: 30-210-772-4710 (S.P.); +44-747-115-5785 (V.K.)

Received: 19 November 2018; Accepted: 8 January 2019; Published: 12 January 2019



**Abstract:** Main target of the present work is to elucidate the effect of both initial microstructure and heating rate on phase transformations that occur during ultrafast processing. For this purpose, two initial microstructures, a ferritic-pearlitic and a soft-annealed microstructure were considered. We applied different heating rates (10 °C/s, 200 °C/s, 300 °C/s) up to the peak austenitization temperature,  $\theta \cong 900$  °C. The evolving microstructure is analysed via SEM and EBSD, whereas the carbide dissolution and austenite formation is simulated with Thermocalc<sup>®</sup> and DICTRA software. Data obtained in this research proves that, when the heating rate increases, the carbide dissolution rate is disseminated. Compared to a conventional heating rate, where the local chemical composition homogenizes as a result of diffusion, rapid reheating leads to intense segregation of the substitutional atoms at the cementite/austenite interface and turns diffusion to a sluggish process. This fact, combined to the infinitesimal time for diffusion, forms an inhomogeneous carbon distribution along the microstructure. This inhomogeneity is further enhanced by the presence of increased carbides' size present in the initial microstructure. Due to rapid heating, these carbides cannot be decomposed since the diffusion distance of alloying elements increases and the diffusion of alloying elements is impeded during ultrafast heating, thus, remain undissolved at peak austenitization temperature. Their presence and effect in heterogeneous ferrite nucleation restrict austenite grain growth. Consequently, fine austenite grains in conjunction with their chemical heterogeneity lead to the coexistence of fine martensite, bainite laths and undissolved carbides in the final microstructure after quenching.

**Keywords:** ultrafast heating; phase transformation; moving boundaries; Dictra; nanostructured steel; martensite/bainite

## 1. Introduction

The application of ultrafast heat treatment or “flash annealing” (rapid heating followed by peak austenitization and water quenching) has been applied as a cost-efficient reheating process for designing steels with strength commensurate to that of advanced high strength steels (AHSS). This process is characterized by rapid thermal cycles with duration less than 10 s [1–5]. The thermal process is divided into three stages. These are: (a) rapid reheating, (b) isothermal processing (at  $T_{\text{peak}}$  for  $t = 2$  s) and (c) rapid cooling (quenching from  $T_{\text{peak}}$  to  $T = 25$  °C). Such an approach is desirable, because it yields to improvement of the mechanical properties due to the wide range of properties that are derived from refined microstructures since its constituents range within submicron to nanoscale. In parallel, no

need exists for heavily alloyed materials and excessively long or complex (two, three or four step) heat treatments [6,7]. Additionally, ultrafast heating is interesting for welding processes, as similar heat cycles are a common ground. The behaviour of the initial microstructure, the role of existing carbides in the austenite nucleation, the effect in deteriorating austenitic grain growth and the possibility to create a different phase transformation evolution path are the significant characteristics of high strength steel welding processes and the related post weld heat treatments [8], [9]. Carbides' dissolution process and local chemical composition are of great significance for modern AHSS such as Q&P, DP and TRIP steels [10–12]. Carbon enrichment of the austenite can occur only under the preliminary condition of carbon trapping minimization in the microstructure. Carbides act as carbon traps and lower locally the C-equivalent eliminating the possibility to retain the austenite during quench to room temperature [11]. Thus, the heat treatment of modern AHSS is of paramount importance for setting a tailored microstructure to proliferate advanced mechanical properties. So far, homogeneous austenite and/or austenite/ferrite starting microstructures were utilized for the development of AHSS, such as DP and TRIP steels. The effect of rapid heating was only utilized in surface hardening for industrial applications [13,14]. However, ultrafast heating followed by quenching has led to mixed martensitic/bainitic/carbides nanostructures responsible for high mechanical properties in a heat treatment cycle, which is similar to this of DP steels but a rapid one. It must be taken into consideration that the initial microstructure of UFH steels is inhomogeneous and consists of very fine austenite and undissolved carbides. The transformation temperatures are also pushed to higher levels influencing also the austenite grain growth, which is of course very limited due to the minimum dwell times at the peak temperature (max. 2 s).

De Knijf et al. [15] studied the effect of high heating rate on the resulting microstructure in Q&P steels and found that it results in refined prior austenite grains and that specimen subjected to increased heating rates presented ductile dimples in fracture surface. Cerda et al. [16,17] investigated the recrystallization behaviour under various heating rates tested between 100–1500 °C/s in cold-rolled low alloy steels. The results have shown that with increasing heating rate texture components are strongly affected. Recrystallization components are rarely found and the components of the cold-deformed microstructure are dominant after rapid heating. Thus, the physically-based process of recrystallization is suppressed with increased heating rate leading to a refined microstructure. The effect of heating rate on austenite transformation has been also rationalized by Kaluba et al. [18], Cerda et al. [19,20] and Papaefthymiou et al. [21]. During rapid heating, lath-shaped austenite was triggered by cementite partial dissolution and C supersaturation at ferrite grain boundaries. The temperature at which massive austenite transformation occurs, can be determined via thermodynamics. Since austenite forms at cementite/ferrite and at ferrite/ferrite interfaces, local C concentration is responsible for changes in the austenite formation mechanism [20]. Recent scientific studies by Cerda et al. [22] and Papaefthymiou et al. [23] have shown that carbides play a significant role in phase transformations during Ultra Fast Heat Treatment (UFHT). When carbides enriched in chromium (Cr) and manganese (Mn) are subjected to rapid heating, their dissolution is impeded since the substitutional atoms Cr and Mn are concentrated in the cementite/austenite interface affecting the diffusion velocity of carbon between cementite and austenite. This in turn causes a retardation on the carbide dissolution and austenite transformation. Segregation of substitutional alloying elements occurs also at isothermal heat treatments, which alters the conditions of local equilibrium affecting the interface motion and the final chemical composition of the steel as also shown by Bhadeshia [24], Ghosh & Olson [25], Miyamoto et al. [26], Ollat et al. [27], Qiu et al. [28], Yamasita et al. [29] and Aranda et al. [30]. Papaefthymiou et al. [23] recently found evidence of the coexistence of martensite and bainite, which was finally correlated to the chemical heterogeneity in the austenite.

Despite considerable work, that has been implemented to understand the microstructural evolution during the ultrafast heating, the effect of initial microstructure is not well defined. In pearlite bands, lamellar cementite tends to fragment to numerous small spherical particles when exposed to high temperatures according to Guo et al. [31], whereas cementite of pearlitic bands, when subjected

to spheroidizing, tends to coarsen as shown by Lupton & Warrington [32]. Recently, the effect of initial microstructure in the final microstructure of quenched and tempered Q&T steels has been rationalized by Eggbauer et al. [33]. Austenitizing-point temperature and chemical composition of austenite deviate between lamellar and spheroidized cementite. However, the heating rate for producing Q&T steels was significantly lower than the one for rapid heating. Therefore, a more thorough study of the effect of initial microstructure and rapid heating on the final microstructure after UFHT is necessary.

The necessity to elucidate the effect of initial microstructure and heating rate in the final microstructure of an UFHT (heating rate  $>100$  °C/s) leads the research to ultrafast heat treatments for a low alloyed chromium (Cr)-molybdenum (Mo) steel. The initial and final microstructures were characterized by means of electron microscopy techniques (SEM) and Electron Backscatter Diffraction (EBSD). The computational approach through Dictra and Thermocalc [34] databases assert the way according to which the initial steel microstructure could affect the diffusion phenomena locally, close enough to the cementite/ferrite interface.

## 2. Materials and Methods

### 2.1. Compositions of the Experimental Steels

For the examination of the CrMo steel microstructure evolution under the rapid heating processes, one steel in two different conditions was used: (a) as-rolled (hot rolled) with a ferritic-pearlitic (FP) microstructure and (b) soft annealed with ferrite and spheroidized cementite (FSC). The chemical composition of the CrMo steel is given in Table 1. The CrMo samples were received as 10 mm cylinders with 3 mm diameter.

**Table 1.** Chemical composition (wt.%) of CrMo low alloyed steel.

Element	C	Mn	Si	Cr	Mo	P	S
%	0.43	1–1.43	0.3–0.4	1.1–1.23	0.1–0.25	<0.040	<0.040

### 2.2. Heat Treatment

The dilatometric experiments implemented under the heating rates of 10 °C/s (conventional heating) and 300 °C/s (ultrafast heating), followed by isothermal holding at the peak austenitization temperature for the time intervals of 2 s (ultrafast experiments) and 300 s (usual heating rate experiments). The quenching stage is completed using helium as a cooling agent. The trials were performed under controlled heating and cooling conditions in a Baehr 805 deformation dilatometer. Table 2 summarizes the experimental data for the heating rates that were implemented to the specimens. The dilatometry analysis delineates the temperatures that ferrite to austenite transformation starts ( $A_1$ ) and the ones that austenitic transformation has been completed ( $A_3$ ). The dilatometry results indicate that a high heating rate can substantially increase the  $A_1$  and  $A_3$  temperatures (Figure 1). These temperatures seem to deviate from the estimated temperatures, which can be found on the phase diagram (Figure 2) and vary along different ultrafast thermal cycles.

### 2.3. Microstructural Characterization

The resulting microstructures were evaluated via scanning electron microscopy (SEM). Misorientation angle analysis was performed via electron backscattered diffraction (EBSD). Each specimen (length: 10 mm, width: 3 mm) was prepared according to the standard procedure by grinding and polishing to 0.3  $\mu\text{m}$  and 0.1  $\mu\text{m}$  using a Mol-B3 and an OPS suspension, for about 5 min, each one. After sample preparation, the etching process followed using an aqueous solution of 2% Nital. SEM and EBSD analysis was performed using a FEI XL40 SFEG-SEM (FEI, Amsterdam, The Netherlands) operated at 20 kV beam current corresponding to FEI spot size 3 for aperture 100  $\mu\text{m}$  and working distance of 10 mm. The EBSD patterns were captured with an EDAX Hikari XP camera operated with

EDAX-TSL-OIM-Data Collection version 6 software (AMETEK, Berwyn, PA, USA) in a hexagonal scan grid with a step size of 90 nm. The orientation data were post-processed using the following grain definition; grain boundary misorientation higher than  $5^\circ$ , minimum 4 pixels per grain and a confidence index (CI) larger than 0.1. In addition, hardness tests (HV) were performed with diamond indent ( $136^\circ$ ) and a load of 300 g.

**Table 2.** Representation of four separate thermal cycles and microstructural characteristics for each one of the samples.

Samples	Thermal Cycles
FP_10	<b>Initial microstructure (as-rolled): ferrite-pearlite (FP),</b> heating rate: $10^\circ\text{C/s}$ , $T_{\text{peak}}$ : $900^\circ\text{C}$ , isothermal holding: 5 min, quenching
FSC_10	<b>Initial microstructure (soft annealed): ferrite-spheroidized carbides (FSC),</b> heating rate: $10^\circ\text{C/s}$ , $T_{\text{peak}}$ : $900^\circ\text{C}$ , isothermal holding: 5 min, quenching
FP_200	<b>Initial microstructure: ferrite-pearlite (FP),</b> heating rate: $200^\circ\text{C/s}$ , $T_{\text{peak}}$ : $900^\circ\text{C}$ , isothermal holding: 5 min, quenching
FSC_300	<b>Initial microstructure: ferrite-spheroidized carbides (FSC),</b> heating rates: $300^\circ\text{C/s}$ , $T_{\text{peak}}$ : $900^\circ\text{C}$ , isothermal holding: 5 min, quenching

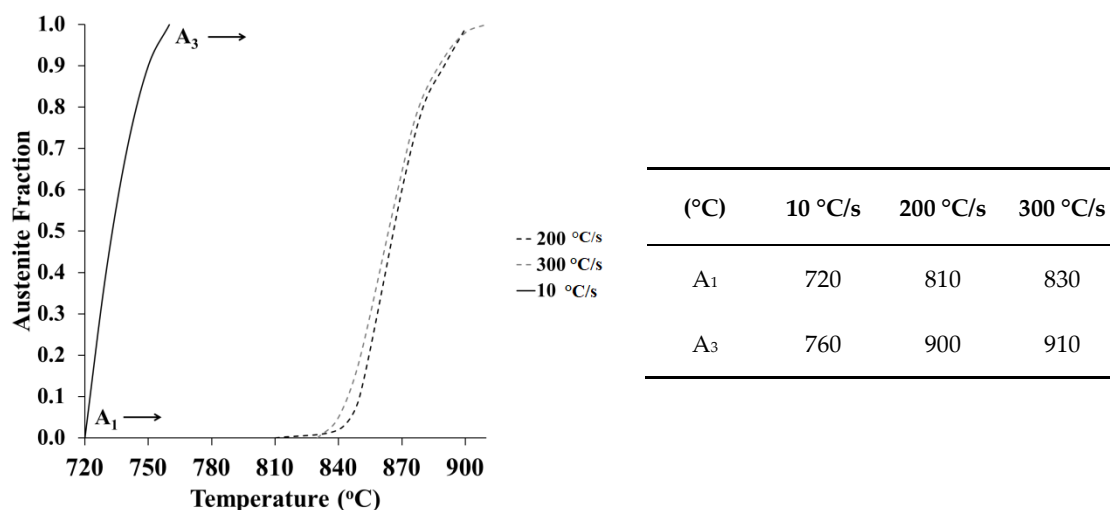


**Figure 1.** Diagram of austenite fraction in the  $\alpha + \gamma$  region as derived from dilatometry curves for  $10^\circ\text{C/s}$  (equilibrium state),  $200^\circ\text{C/s}$  and  $300^\circ\text{C/s}$  heating rates. Temperatures  $A_1$  and  $A_3$  that were increased are closely related to heating rate increasing pattern.

#### 2.4. Modelling of the Microstructure

In order to rationalize the microscopy results and understand the phase transformations at conditions unfavourable for solid state diffusion, two different ultrafast heating rates were examined,  $200^\circ\text{C/s}$  and  $300^\circ\text{C/s}$  contradicting these to a  $10^\circ\text{C/s}$  a conventional rate. Thermocalc and Dictra databases, TCFE8 and MOBFE3 respectively, substantiated the simulations for the CrMo steel and the alterable magnitude of the carbides for the aforementioned steel compositions. Using DICTRA, dissolution of cementite, ferrite to austenite transformation and chemical gradients across interfaces between cementite and the matrix ( $\alpha/\gamma$ ) were studied during rapid heating up to  $900^\circ\text{C}$ . In order to evaluate the effect of initial microstructure during ultrafast heating, we assumed that the carbides are spherical with a 5 nm diameter corresponding to initial ferritic/pearlitic microstructure and a 200 nm to 500 nm diameter corresponding to the initial soft-annealed microstructure. Since  $200^\circ\text{C/s}$  and  $300^\circ\text{C/s}$  heating rates affect austenite transformation (Figure 1), the heating rate of  $200^\circ\text{C/s}$  was selected for the dissolution of carbides with sizes from 200 nm to 500 nm. The chemical composition for each phase was determined in equilibrium state ( $\theta = 500^\circ\text{C}$ ) via Thermocalc<sup>®</sup> by taking the volume

fractions of the components into consideration (Table 3). Since transformation temperatures shift at higher values by increasing the heating rate, results obtained from the dilatometry, such as the actual  $A_1$  and  $A_3$  of austenite transformation, as designated in the dilatometry curve in Figure 1, are used as an input in the simulation. At the interfaces of carbides with ferrite or austenite thermodynamic equilibrium was assumed (local equilibrium hypothesis). At  $A_1$ , the austenite is set to nucleate and grow at the interface of carbides with ferrite.

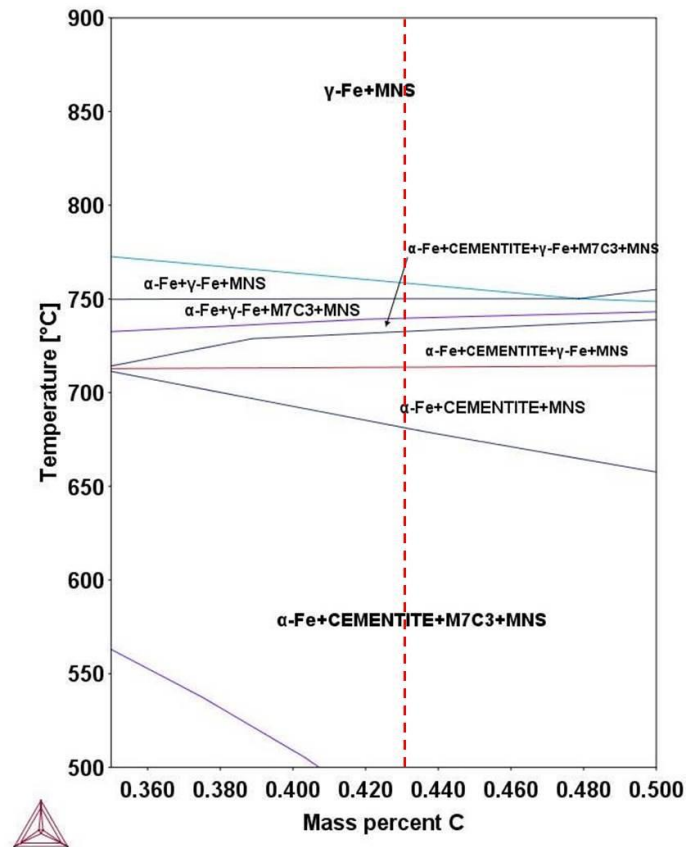


**Figure 2.** Isopleth of the phase diagram of CrMo steel calculated using Thermocalc<sup>®</sup> software. The dashed line indicates the carbon (C) content. The equilibrium  $A_1$  and  $A_3$  temperatures are defined also (720 °C and 760 °C respectively).

**Table 3.** Initial chemical compositions of cementite (5 nm, 200 nm, 500 nm) and ferrite calculated at 500 °C.

Phases	C (wt.%)	Cr (wt.%)	Mn (wt.%)	Mo (wt.%)
Cementite	6.67	9.17	9.69	0.17
Ferrite	0.0007	0.073	0.29	0.018

The computational process is determined on the one-dimensional space in which certain finite elements methods, such as the Euler method were utilized in order to simulate the diffusion of alloying elements C, Cr, Mn and Mo through an interface between the regions of cementite and ferrite and between the regions of cementite and austenite.

### 3. Results

#### 3.1. Microstructural Analysis

Figure 3 depicts the SEM micrographs of all tested specimens. Samples FP\_10 and FSC\_10 (Figure 3a,b) produce different microstructures after quenching despite the fact that they were subjected

to the same thermal cycle. The microstructure of FP\_10 (Figure 3a) consists of martensitic laths with length up to 20  $\mu\text{m}$ , whereas FSC\_10 (Figure 3b) consists of martensitic laths, while small globular particles, which represent spherical carbides are discernible in the submicron scale. Samples FP\_200 and FSC\_300 (Figure 3c,d) also produce different microstructures after the UFHT. Sample FP\_200 (Figure 3c) obtains martensitic laths with length smaller than 8  $\mu\text{m}$ , whereas sample SF\_300 (Figure 3d) consists of refined martensitic laths ranging less than 5  $\mu\text{m}$ . Compared to the other samples, the presence of spheroidized carbides is more intense than in the “FSC\_10.”

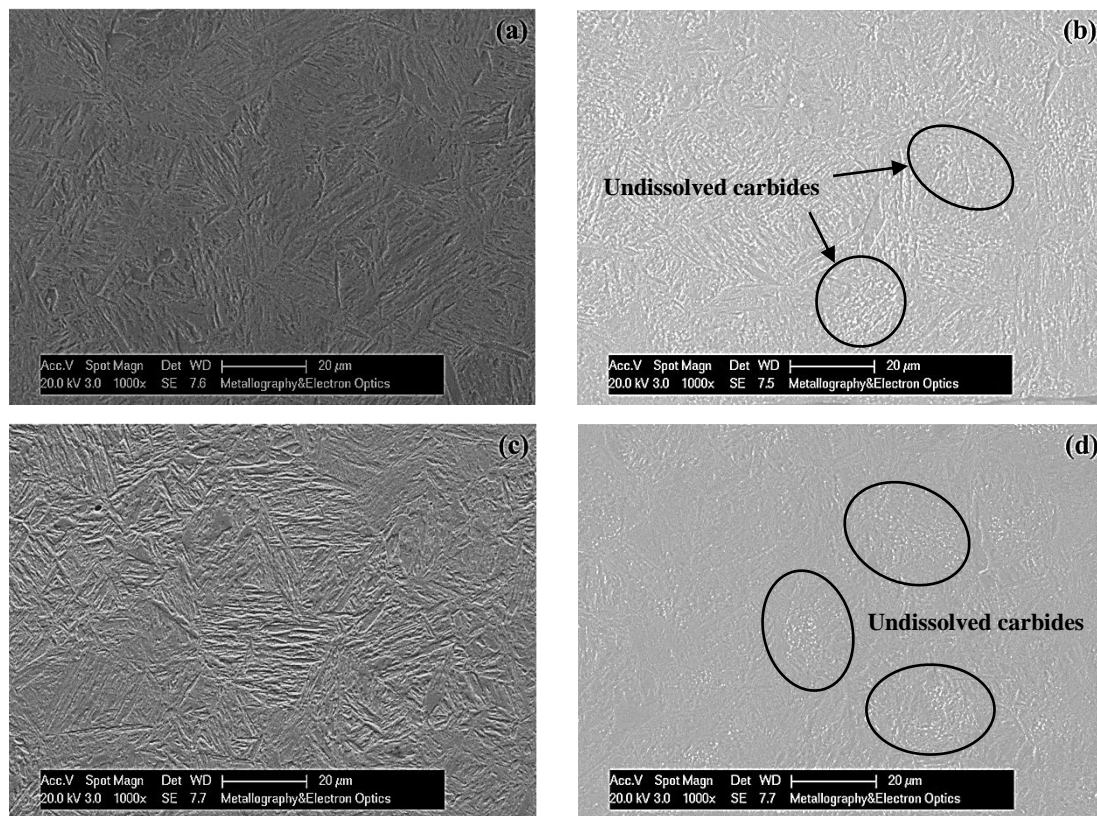


**Figure 3.** SEM micrographs obtained from (a) FP\_10, (b) SF\_10, (c) FP\_200 and (d) FSC\_300.

Using Electron Backscattered Diffraction (EBSD) the angle boundaries between martensite laths were specified. Furthermore, the Prior Austenite Grain Boundaries Size (PAGS) was determined. According to Kurdjumov-Sachs (KS) crystallographic relationship, certain misorientation angles exist and are used for the discrimination of parent austenite and martensite grain boundaries. The martensite boundaries could be determined from  $10^\circ$  to  $20^\circ$  and  $47^\circ$  to  $57^\circ$  in the case of packets and from  $50^\circ$  to  $60^\circ$  misorientation angles in the case of blocks. Misorientation angles from  $20^\circ$  to  $47^\circ$  correspond to former austenite grains according to Hata et al. [35]. The evaluation of the misorientation angles corresponding to prior austenite grains (Figure 4) indicates that at  $10^\circ\text{C/s}$  heating rate the former austenite grains range between 7–10  $\mu\text{m}$  (Figure 4a,b). Similar results were observed when the ferritic-pearlitic samples were heated at  $200^\circ\text{C/s}$  in which the austenite grains were measured at 11  $\mu\text{m}$  (Figure 4c), whereas the austenite grain size was substantially decreased at 5  $\mu\text{m}$  when the sample was subjected to  $300^\circ\text{C/s}$  (Figure 4d). The hardness values measured after heat treatment are shown in Figure 5. The FSC samples present higher hardness values similar to the martensitic values of FSC\_300 specimen as it presents the finer PAGS therefore the final microstructure after quenching would be refined. Also the homogeneously distribution of carbides may result in increased hardness. The FP samples present lower hardness, which is similar to lower bainite according to Wang et al. [36] and it is attributed to the presence of coarser laths.

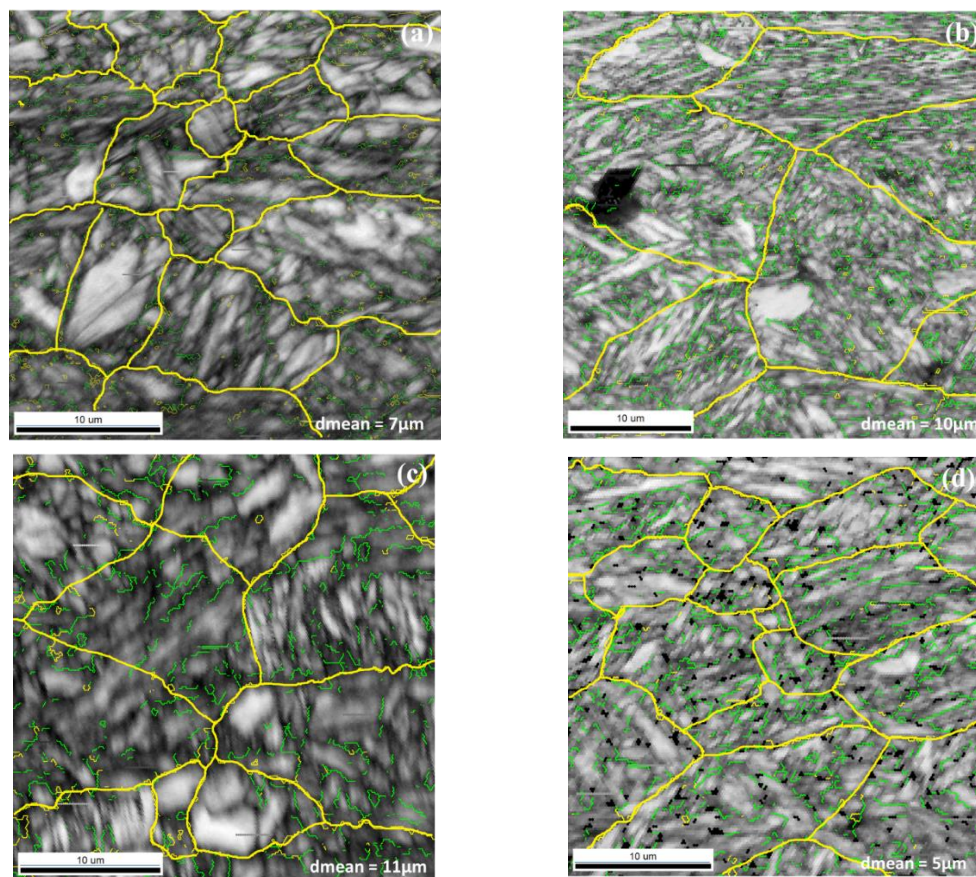


**Figure 4.** Misorientation map obtained from EBSD from (a) FP\_10, (b) FSC\_10, (c) FP\_200 and (d) FSC\_300 showing the mean values of PAGS. The green lines indicate misorientation angles of 50–60° which correspond to bainitic ferrite laths.

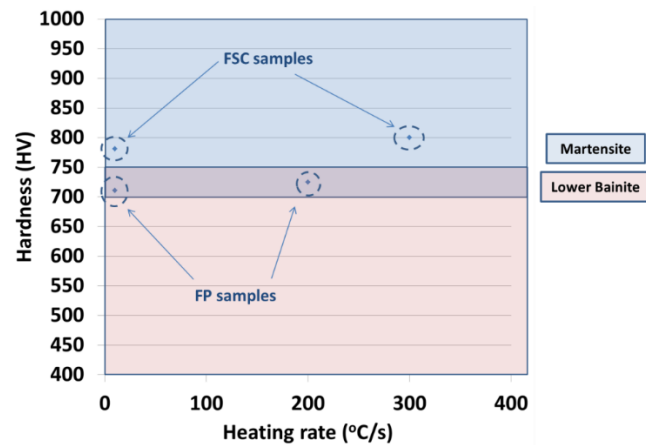


**Figure 5.** Hardness measurements of each sample in conjunction with heating rate. The hardness range of martensite (750–1000 HV) and lower bainite (400–750 HV) are based on the work of Wang et al. [36].

### 3.2. Modelling Results

Figure 6 depicts the chemical gradients near the cementite/austenite interface for each sample in the  $\alpha + \gamma$  region. A quantitative analysis to determine modelling results has signified the increase of the heating and the accumulation of substitutional alloying elements on the interface among the phases cementite and austenite. Phenomena like the accumulation of these elements eliminate the carbon diffusivity from one phase to another. In the first two seconds of the process, interfacial velocity of the system has been increased reinforcing the substitutional atoms' motion over the carbide/ferrite

interface. When the kinetic system reaches a steady state, such as the isothermal region (up to  $\theta = 900\text{ }^{\circ}\text{C}$ ), interfacial velocity diminishes according to prominent research that has implemented by Cahn J. [37]. This diffusion system is governed by substitutional elements' motion on par with the partitioning local equilibrium (PLE) mechanism and the diffusivity of carbon is degraded relatively with the domination of the substitutional elements, bolstering the total drag effect as Yamasita et al. have stated before [29].

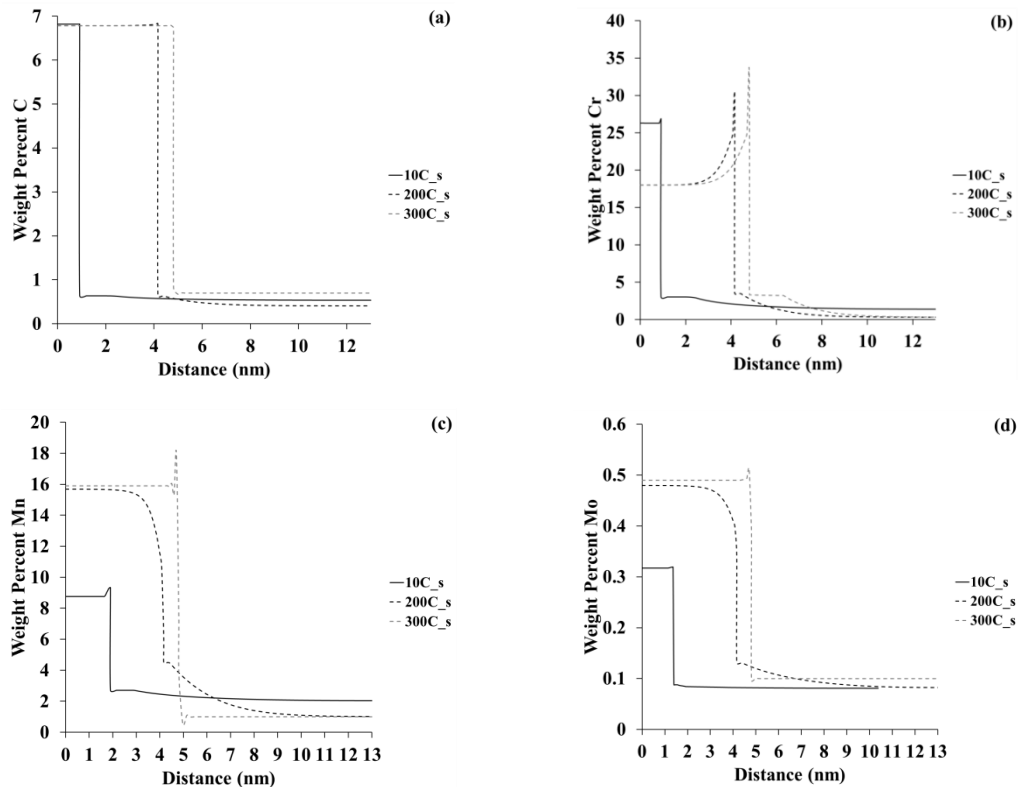


**Figure 6.** Diagrams of (a) carbon, (b) chromium, (c) manganese, (d) molybdenum concentration at the interface of cementite and austenite depending on heating rate at various temperatures within the  $\alpha + \gamma$  region.

Furthermore, Cr affects the motion of carbon atoms during the reheating stage due to the ultrafast processing. Chromium as an alloying element creates a steep line on the interface between the cementite and austenite regions (Figure 6b). This phenomenon ensures the appearance of the local equilibrium mechanism, which affects the velocity of interstitial elements eliminating their motion through the interface and gives an advantage to the motion of substitutional elements, such as Cr, Mn and Mo as also discussed by Ghosh and Olson [25]. The system is dominated by the motion of the substitutional elements and prior distinctions confirm that the solid solution system impedes the carbide dissolution according to Offermann et al. [38] and Calcagnotto et al. [39].

The percentage of Mn is possible to be diminished on the interface, because the Mn atoms are prone to the creation of a bond with the Fe atoms and hinder the carbon diffusion into the austenite (Figure 6c). Furthermore, Mo atoms could create a solute drag phenomenon on the ferrite grain boundaries (Figure 6d). Despite the large radius of Mo atoms, diffusion of these atoms into the austenitic grains has been also detected by Qiu et al. [28]. The Mo concentration on the interface can bolster the appearance of molybdenum carbides (MoC) under the prerequisite that the concentration of carbon should be close to 1 wt.%

## 4. Discussion

### 4.1. Effect of Rapid Heating on the Phase Transformation Evolution

The computational results from Dictra indicate certain effects of the substitutional alloying elements for both ultrafast and conventional heating rates. The Equation (1) describes the system stabilization and the homogeneous distribution of the alloy elements C, Cr, Mn and Mo after the completion of the austenitic transformation, in which  $c^{\gamma\alpha}$  is determined as the concentration of alloying elements that has been diffused from austenite to ferrite and  $c^{\alpha\gamma}$  as the concentration of the atoms that implement the reverse route from ferrite to the formed austenite. As  $c$  the difference between the concentrations  $c^{\gamma\alpha}$  and  $c^{\alpha\gamma}$  is presented;  $\bar{c}$  represents the general concentration of any of the preceded elements in the initial system before any transformation; and  $z$  is a parameter closely linked to the concentration, which receives the value  $z^*$  on the interface between the ferrite and austenite regions according to Andersson and Agren [34].

$$(c^{\alpha\gamma} - \bar{c})z^* = 1/2(\bar{c} - c^{\gamma\alpha})\Delta z \quad (1)$$

The flow of M substitutional atom through the interface, during the austenitic transformation, have to be equal with the diffusion rate in the transformed phase and this is identified mathematically through the following Equation (2) [34] in which  $D_C^\gamma$  is the diffusion coefficient for carbon (C) in austenite.

$$(c^{\gamma\alpha} - c^{\alpha\gamma})\frac{\partial z^*}{\partial t} = -D_C^\gamma \frac{\partial c}{\partial t} \cong D_C^\gamma \frac{\bar{c} - c^{\gamma\alpha}}{\Delta z} \quad (2)$$

In conventional heating the parameter of time  $t$ , as illustrated in the Equation (2), is sufficient for the diffusion of carbon and the substitutional elements in the system with the interface to implement slow motion. Figure 4a,b indicate that the austenite grains before the quenching have been augmented due to the slow reheating and the extensive isothermal holding at the austenitization temperature. On the contrary, Figure 4c,d show that the austenite grains are smaller in size since the increased heating rate shifts the  $A_1$  and  $A_3$  temperatures to higher values and the  $T_{\text{peak}}$  is the new  $A_3$  temperature so the driving force for the austenite grain growth depends only on the holding time and not in the temperature increase as it occurs in conventional heating.

The Equations (3) and (4) describe the motion of interstitial (C) and substitutional (M) element into the system, as Aaron et al. [40] have described using Zener's approximation, in accordance with their diffusion coefficients, diffusion velocities and the differences of the concentrations between the two regions, ferrite and austenite:

$$(c_C^{\gamma\alpha} - c_C^{\alpha\gamma}) \cdot v_C = -D_C^\gamma \nabla c_C \quad (3)$$

$$(c_M^{\gamma\alpha} - c_M^{\alpha\gamma}) \cdot v_M = -D_M^\gamma \nabla c_M \quad (4)$$

where  $c_C^{\gamma\alpha}$ ,  $c_M^{\gamma\alpha}$  represent the concentrations of C and M, which are diffused from austenite to ferrite through the interface and  $c_C^{\alpha\gamma}$ ,  $c_M^{\alpha\gamma}$  represent the concentrations of the same elements, that are diffused from ferrite to austenite through the interface. The  $v$  symbolizes the velocity and  $D^\gamma$  the diffusion coefficient of C and M elements.

The Cr, Mn or Mo, as substitutional atoms, hinder the diffusion of C and are characterized from lower diffusion coefficients than this of C, which is an interstitial atom. These lower diffusion coefficients contribute to smaller velocities of the substitutional elements through the interface according to the Equations (3) and (4). The substitutional alloying elements have been redistributed into the matrix alleviating micro-segregation and augmenting grains' radius.

Furthermore, the local equilibrium enhances the mobility of the substitutional atoms disseminating the C flow and delays the ferrite-to-austenite transformation leading to an augmentation of prior austenite grain boundaries. With the heating rate's increase, the accumulation of substitutional elements near

the cementite/austenite interface becomes more intense. Under these circumstances, Mn and Cr atoms are detected to incorporate a motion in two different directions through the interface (Figure 6b–d). The normal motion of these elements has been carried out from cementite to ferrite or from cementite to austenite and to the reverse direction, which is from ferrite to cementite or from austenite to ferrite as discussed by Caballero et al. [41].

The increased concentration of Cr atoms close to carbide/austenite interface in combination with Cr strong affinity with C could lead to impediment of interface migration whereas it could be an indication for solute drag effect [28]. Papaefthymiou et al. [23] had proved that the accumulation of substitutional atoms near the carbide/austenite interface decreases the interface velocity and hinders the austenitic transformation during rapid heating as also stated by Miyamoto et al. [26] and Wang et al. [36]. However, solute drag effect, as defined by the work of Cahn [37], Hillert and Sundman [42], states, that not only the segregation of impurities or solute atoms but also the diffusivity within the grain boundary, can slow the boundary migration rate. Although this approach is interesting, further research on the characteristics of solute drag has to be implemented, in order to fathom out the segregation phenomena during rapid heating.

In addition, Mn can lower the  $A_1$  and  $A_3$  temperatures, which could enable the formation of austenite at lower temperatures. Furthermore, Mo atoms could create solute drag phenomenon on the grain boundaries of austenite.

In case of ultrafast heating, the limited time for diffusion as well as the segregation of substitutional atoms lead to the presence of undissolved carbides at  $T_{\text{peak}}$ . This effect is shown in Figure 7, which depicts the dissolution of cementite in conjunction with both temperature and heating rate. After the holding time at the peak temperature, the undissolved carbides in both occasions act as nucleation sites, which will lead to an ultrafine final microstructure. The carbides support the creation of new phases, such as bainite, mixed with martensite laths during the quenching process as discussed by Caballero et al. [41] and Sharma et al. [43]. The local chemical composition of the material after the ultrafast process is a crucial issue, because the local chemical compositions could affect the rate and temperature, by which phase transformations occur. In this way, the phases or the microstructural constituents of the final microstructure are created as a consequence of different diffusion rates of the alloying elements as discussed by Goulas et al. [44] and Hidalgo et al. [45].

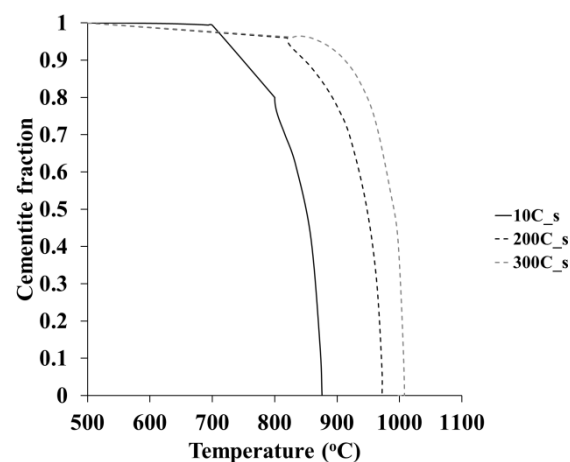


Figure 7. Diminution of cementite size related to heating rate and temperature.

#### 4.2. Effect of Initial Microstructure

SEM analysis after the completion of a conventional and an ultrafast heat treatment including both initial microstructures has been implemented. The analysis emphasizes on the as-rolled ferritic-pearlitic (FP) and the soft annealed ferrite with spheroidized carbides (FSC) microstructure respectively, revealing the presence of quite different final microstructures. During ultrafast annealing the banded

cementite within pearlite is divided and the resulting fragmented carbides alter their geometry, obtaining the spherical one similarly to results shown by Aranda et al. [30] and Calcagnotto et al. [39]. The initial FSC microstructure presents coarse carbides due to prolonged soaking at the spheroidization temperature ( $T_{\text{sph}} < A_1$ ) in case of spheroidization annealing similar to microstructures presented by Lupton et al. [32]. Fluctuating carbide size was expected to lead to a different outcome of the phase transformations during UFHT and in variations in the final microstructures. The final microstructures after UFHT, which derived from the FP initial microstructure did not contain any undissolved carbides (Figure 3c), whereas the ones derived from the FSC initial microstructure contained partially dissolved carbides (Figure 3d). Figure 8 shows that coarser cementite (200 nm and 500 nm) exhibits significantly lower dissolution rate than fine cementite, when exposed to rapid heating. The slower dissolution rate can be explained with Equation (5) in which  $v_{\theta/\gamma}$  is the velocity movement of interface cementite/austenite,  $D_k$  the diffusion coefficient ( $\text{m}^2/\text{s}$ ) of element  $k$ ,  $x_k^{\theta/\gamma}$  mole fraction of element  $k$  of phase  $\theta$  at the interface  $\theta/\gamma$ ,  $x_k^{\gamma/\alpha}$  mole fraction of element  $k$  of phase  $\gamma$  at the interface  $\gamma/\alpha$ ,  $z$  the effective diffusion in carbides,  $x_k^\gamma$  mole fraction of element  $k$  of phase  $\gamma$ ,  $x_k^\theta$  mole fraction of element  $k$  of phase  $\theta$  [23].

$$v_{\theta/\gamma} = \frac{D_k(x_k^{\theta/\gamma} - x_k^{\gamma/\alpha})}{z(x_k^\gamma - x_k^\theta)} \quad (5)$$

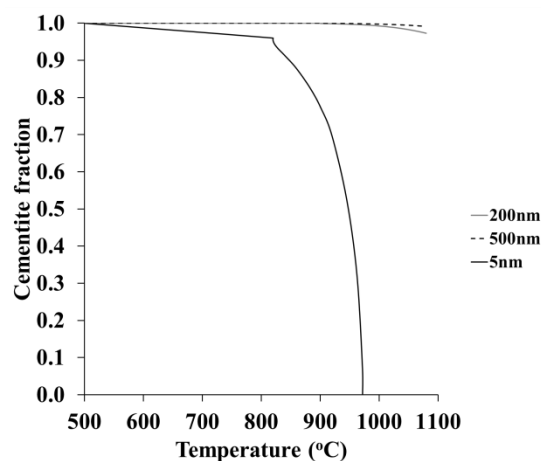


**Figure 8.** Examining cementite dissolution according to the initial size of carbides into the microstructure. It was identified that as carbides' size increases, dissolution rate tends to be diminished during a 5 s heating stage. Significant shrinking was detected only for carbides with 5 nm size.

According to Equation (5) the velocity of interface motion is inversely proportional to the diffusion distance. The increase of the diffusion distance of the alloying elements in combination with the short time for diffusion, leads to a decrease of the interface velocity and the cementite dissolution is impeded.

## 5. Conclusions

In this study the effect of both initial microstructure and heating rate on the microstructure gained after ultrafast processing was investigated and analysed. The evolution of carbide dissolution and austenite formation are considered to have a significant impact on the final microstructure.

Comparing the effect of heating rate with the carbide dissolution rate, it is concluded that ultrafast heating rates (200 °C/s and 300 °C/s) impeded the motion of the carbon atoms through an interface. When conventional heating rate (10 °C/s) was utilized, complete carbide dissolution occurred. Intense segregation of substitutional atoms near cementite/austenite was found as the heating rate increases. This fact leads to no or partial carbide dissolution and leads to chemical heterogeneity in the austenite matrix. This in turn alters locally the transformation temperatures of bainite and martensite during quenching.

In initial microstructures that exhibit coarser carbides it is more difficult to achieve complete carbide dissolution compared to others containing fine carbides. Therefore, the microstructures with coarser carbides such as soft annealed microstructures have a larger fraction of undissolved carbides at peak austenitizing temperatures.

Rapid heating process generates finer austenite grains compared to conventional heating rates during peak austenitization. The existence of undissolved carbides at austenitizing temperature is considered as the motive for austenite's nucleation sites formation and prevents austenite's grain growth. The maintenance of fine austenite grains prior to quenching coalescing the undissolved carbides leads to finer martensitic/bainitic laths in the final microstructure after UFHT.

The behaviour of the carbide dissolution and the phase transformation evolution is of great significance for welding and AHSS processing, especially for Q&P, DP, TRIP and Q&T steels when these are subjected to ultrafast heating.

The understanding of the microstructure evolution under ultrafast heating and a heterogeneous chemical composition of the austenite before the quenching stage can contribute to the development of ultrafast processed ultrafine grained DP steels with improved mechanical properties.

**Author Contributions:** We describe contributions to the paper using the CRediT (Contributor Roles Taxonomy). Conceptualization: S.P.; Methodology: S.P. and M.B.; Software: V.K. & M.B.; Validation: V.K. & M.B.; Formal Analysis: V.K. & M.B.; Investigation: V.K. & M.B.; Resources: V.K. & M.B.; Data Curation: V.K., M.B.; Writing—Original Draft Preparation: V.K.; Writing—Review & Editing: V.K., M.B. and S.P.; Visualization: V.K., M.B.; Supervision: M.B. and S.P.; Project Administration: S.P.

**Funding:** This research did not receive any specific grant from funding agencies in the public, commercial or non-for-profit sectors.

**Acknowledgments:** The work described in this article was supported by the Hellenic Research Centre for Metals S.A (ELKEME S.A). The authors would like to acknowledge C. Goulas for the provision of the soft annealed 42MnCr6 steel for dilatometric experiments.

**Conflicts of Interest:** The authors declare no conflict of interest.

## References

1. Lolla, S.V.T. Understanding Microstructure Evolution in Rapid Thermal Processing of AISI 8620 Steel. Ph.D. Dissertation, The Ohio State University, Columbus, OH, USA, 2009.
2. Lolla, T.; Alexandrov, B.; Babu, S.; Cola, G. Towards understanding the microstructure development during heating and cooling of steels. In Proceedings of the THERMEC '09, Berlin, Germany, 25–29 August 2009.
3. Lolla, T.; Cola, G.; Narayanan, B.; Alexandrov, B.; Babu, S.S. Development of rapid heating and cooling (flash processing) process to produce advanced high strength steel microstructures. *Mater. Sci. Technol.* **2011**, *27*, 863–875. [[CrossRef](#)]
4. Papaefthymiou, S. A New Opportunity for the Design of Advanced High Strength Steels with Heterogeneous-Phase Microstructures via Rapid Thermal Processing. *J. Nanosci. Adv. Tech.* **2017**, *2*, 20–23. [[CrossRef](#)]
5. Cola, G. Properties of bainite nucleated by water quenching in 80 ms. In *1st International Symposium on Steel Science*; Iron and Steel Institute of Japan: Tokyo, Japan, 2007.
6. Zhao, J.; Jiang, Z. Thermomechanical processing of advanced high strength steels. *Prog. Mater. Sci.* **2018**, *94*, 174–242. [[CrossRef](#)]
7. Zhang, J.; Fu, R.; Zhang, M.; Liu, R.; Wei, X.; Li, L. Bake hardening behaviour of TRIP and DP steels. *J. Univ. Sci. Technol. Beijing* **2008**, *15*, 132–137. [[CrossRef](#)]
8. Dong, H.; Hao, X.; Deng, D. Effect of Welding Heat Input on Microstructure and Mechanical Properties of HSLA Steel Joint. *Metallogr. Microstruct. Anal.* **2014**, *3*, 138–146. [[CrossRef](#)]
9. Li, H.; Liu, D.; Yan, Y.; Guo, N.; Liu, Y.; Feng, J. Effects of heat input on arc stability and weld quality in underwater wet flux-cored arc welding of E40 steel. *J. Manuf. Process.* **2018**, *31*, 833–843. [[CrossRef](#)]
10. Bleck, W.; Papaefthymiou, S.; Frehn, A. Microstructure and Tensile Properties in Dual Phase and Trip Steels. *Steel Res. Int.* **2004**, *75*, 704–710. [[CrossRef](#)]

11. Zhang, H.; Ponge, D.; Raabe, D. Designing quadplex (four-phase) microstructures in an ultrahigh carbon steel. *Mater. Sci. Eng. A* **2014**, *612*, 46–53. [[CrossRef](#)]
12. Adamczyk, J.; Opiela, M. Influence of the thermo–mechanical treatment parameters on the inhomogeneity of the austenite structure and mechanical properties of the Cr–Mo steel with Nb, Ti and B microadditions. *J. Mater. Process. Technol.* **2004**, *157*, 456–461. [[CrossRef](#)]
13. Rudnev, V.; Loveless, D.; Cook, R. *Handbook of Induction Heating*; Marcell Dekker Inc.: New York, NY, USA, 2003.
14. Zinn, S.; Semiatin, S. *Elements of Induction Heating: Design, Control, and Applications*; EPRI, ASM International: Metals Park, OH, USA, 1988.
15. De Knijf, D.; Puype, A.; Föjler, C.; Petrov, R. The influence of ultra-fast annealing prior to quenching and partitioning on the microstructure and mechanical properties. *Mater. Sci. Eng. A* **2015**, *627*, 182–190. [[CrossRef](#)]
16. Cerda, F.M.C.; Goulas, C.; Sabirov, I.; Papaefthymiou, S.; Monsalve, A.; Petrov, R. Microstructure, texture and mechanical properties in a low carbon steel after ultrafast heating. *Mater. Sci. Eng. A* **2016**, *672*, 108–120. [[CrossRef](#)]
17. Cerda, F.M.C.; Kestens, L.; Monsalve, A.; Petrov, R. The Effect of Ultrafast Heating in Cold-Rolled Low Carbon Steel: Recrystallization and Texture Evolution. *Metals* **2016**, *6*, 288. [[CrossRef](#)]
18. Kaluba, W.; Taillard, R.; Foct, J. The bainitic mechanism of austenite formation during rapid heating. *Acta Mater.* **1998**, *46*, 5917–5927. [[CrossRef](#)]
19. Cerda, F.C.; Sabirov, I.; Goulas, C.; Sietsma, J.; Monsalve, A.; Petrov, R. Austenite formation in 0.2% C and 0.45% C steels under conventional and ultrafast heating. *Mater. Des.* **2017**, *116*, 448–460. [[CrossRef](#)]
20. Cerda, F.M.C.; Schulz, B.; Papaefthymiou, S.; Artigas, A.; Monsalve, A.; Petrov, R.H. The Effect of Ultrafast Heating on Cold-Rolled Low Carbon Steel: Formation and Decomposition of Austenite. *Metals* **2016**, *6*, 321. [[CrossRef](#)]
21. Papaefthymiou, S.; Goulas, C.; Cerda, F.M.C.; Geerlofs, N.; Petrov, R. The Effect of Heating Rate on the Microstructure of a Soft-Annealed Medium Carbon Steel. *Steel Res. Int.* **2017**, *88*, 1700158. [[CrossRef](#)]
22. Cerda, F.M.C.; Vercruyssen, F.; Goulas, C.; Schulz, B.; Petrov, R.H. ‘Flash’ Annealing in a Cold-Rolled Low Carbon Steel Alloyed With Cr, Mn, Mo and Nb: Part I—Continuous Phase Transformations. *Steel Res. Int.* **2018**. [[CrossRef](#)]
23. Papaefthymiou, S.; Bouzouni, M.; Petrov, R.H. Study of Carbide Dissolution and Austenite Formation during Ultra-Fast Heating in Medium Carbon Chromium Molybdenum Steel. *Metals* **2018**, *8*, 646. [[CrossRef](#)]
24. Bhadeshia, H.K.D.H. Considerations of solute-drag in relation to transformations in steels. *J. Mater. Sci.* **1983**, *18*, 1473–1481. [[CrossRef](#)]
25. Ghosh, G.; Olson, G.B. Simulation of paraequilibrium growth in multicomponent systems. *Metall. Mater. Trans. A* **2001**, *32*, 455–467. [[CrossRef](#)]
26. Miyamoto, G.; Usuki, H.; Li, Z.-D.; Furuhashi, T. Effects of Mn, Si and Cr addition on reverse transformation at 1073K from spheroidized cementite structure in Fe–0.6 mass% C alloy. *Acta Mater.* **2010**, *58*, 4492–4502. [[CrossRef](#)]
27. Ollat, M.; Militzer, M.; Massardier, V.; Fabrègue, D.; Buscarlet, E.; Keovilay, F.; Perez, M. Mixed-mode model for ferrite-to-austenite phase transformation in dual-phase steel. *Comput. Mater. Sci.* **2018**, *149*, 282–290. [[CrossRef](#)]
28. Qiu, C.; Zurob, H.; Hutchinson, C.; Hutchinson, C. The coupled solute drag effect during ferrite growth in Fe–C–Mn–Si alloys using controlled decarburization. *Acta Mater.* **2015**, *100*, 333–343. [[CrossRef](#)]
29. Yamashita, T.; Enomoto, M.; Tanaka, Y.; Matsuda, H.; Nagoshi, M. Analysis of Carbon Partitioning at an Early Stage of Proeutectoid Ferrite Transformation in a Low Carbon Mn–Si Steel by High Accuracy FE-EPMA. *ISIJ Int.* **2018**, *58*, 1079–1085. [[CrossRef](#)]
30. Aranda, M.; Rementeria, R.; Poplawsky, J.; Urones-Garrote, E.; Capdevila, C. The role of C and Mn at the austenite/pearlite reaction front during non-steady-state pearlite growth in a Fe–C–Mn steel. *Scr. Mater.* **2015**, *104*, 67–70. [[CrossRef](#)]
31. Zhang, G.-H.; Chae, J.-Y.; Kim, K.-H.; Suh, D.W. Effects of Mn, Si and Cr addition on the dissolution and coarsening of pearlitic cementite during intercritical austenitization in Fe–1mass%C alloy. *Mater. Charact.* **2013**, *81*, 56–67. [[CrossRef](#)]
32. Lupton, D.F.; Warrington, D.H. The Influence of Deformation on the Spheroidization and Coarsening of Pearlite. *Met. Sci. J.* **1972**, *6*, 200–204. [[CrossRef](#)]

33. Eggbauer, A.; Lukas, M.; Prevedel, P.; Panzenböck, M.; Ressel, G.; Ebner, R. Effect of Initial Microstructure, Heating Rate and Austenitizing Temperature on the Subsequent Formation of Martensite and Its Microstructural Features in a QT Steel. *Steel Res. Int.* **2018**. [[CrossRef](#)]
34. Andersson, J.-O.; Ågren, J. Models for numerical treatment of multicomponent diffusion in simple phases. *J. Appl. Phys.* **1992**, *72*, 1350–1355. [[CrossRef](#)]
35. Hata, K.; Fujiwara, K.; Wakita, M.; Kawano, K. *Development of a Reconstruction Method of Prior Austenite Microstructure Using EBSD Data of Martensite*; Nippon Steel & Sumitomo Metal Corporation: Tokyo, Japan, 2017.
36. Wang, X.; Zurob, H.S.; Xu, G.; Ye, Q.-B.; Bouaziz, O.; Embury, D. Influence of Microstructural Length Scale on the Strength and Annealing Behavior of Pearlite, Bainite and Martensite. *Metall. Mater. Trans. A* **2012**, *44*, 1454–1461. [[CrossRef](#)]
37. Cahn, J.W. The impurity-drag effect in grain boundary motion. *Acta Metall.* **1962**, *10*, 789–798. [[CrossRef](#)]
38. Offerman, S.; Van Wilderen, L.; Van Dijk, N.; Sietsma, J.; Rekveldt, M.; Van Der Zwaag, S. In-situ study of pearlite nucleation and growth during isothermal austenite decomposition in nearly eutectoid steel. *Acta Mater.* **2003**, *51*, 3927–3938. [[CrossRef](#)]
39. Calcagnotto, M.; Ponge, D.; Raabe, D. On the Effect of Manganese on Grain Size Stability and Hardenability in Ultrafine-Grained Ferrite/Martensite Dual-Phase Steels. *Metall. Mater. Trans. A* **2011**, *43*, 37–46. [[CrossRef](#)]
40. Aaron, H.B.; Fainstein, D.; Kotler, G.R. Diffusion-Limited Phase Transformations: A Comparison and Critical Evaluation of the Mathematical Approximations. *J. Appl. Phys.* **1970**, *41*, 4404–4410. [[CrossRef](#)]
41. Caballero, F.; Miller, M.K.; Garcia-Mateo, C.; Capdevila, C.; De Andrés, C.G. Phase transformation theory: A powerful tool for the design of advanced steels. *JOM* **2008**, *60*, 16–21. [[CrossRef](#)]
42. Hillert, M.; Sundman, B. A treatment of the solute drag on moving grain boundaries and phase interfaces in binary alloys. *Acta Metall.* **1976**, *24*, 731–743. [[CrossRef](#)]
43. Sharma, S.; Nanda, T.; Adhikary, M.; Venugopalan, T.; Kumar, R. A simulation study of pearlite to austenite transformation kinetics in rapidly heated hot-rolled low carbon steel. *Mater. Des.* **2016**, *107*, 65–73. [[CrossRef](#)]
44. Goulas, C.; Mecozzi, M.G.; Sietsma, J. Bainite Formation in Medium-Carbon Low-Silicon Spring Steels Accounting for Chemical Segregation. *Metall. Mater. Trans. A* **2016**, *47*, 3077–3087. [[CrossRef](#)]
45. Hidalgo, J.; Santofimia, M.J.; Hidalgo-García, J. Effect of Prior Austenite Grain Size Refinement by Thermal Cycling on the Microstructural Features of As-Quenched Lath Martensite. *Metall. Mater. Trans. A* **2016**, *47*, 5288–5301. [[CrossRef](#)]



© 2019 by the authors. Licensee MDPI, Basel, Switzerland. This article is an open access article distributed under the terms and conditions of the Creative Commons Attribution (CC BY) license (<http://creativecommons.org/licenses/by/4.0/>).